33RD CONGRESS
OF THE INTERNATIONAL COUNCIL
OF THE AERONAUTICAL SCIENCES
STOCKHOLM, SWEDEN, 4-9 SEPTEMBER, 2022

ICAS
2022
SWEDEN

EXPERIMENTAL INVESTIGATIONS OF AN AEROELASTIC WIND TUNNEL MODEL FOR TAIL BUFFETING ANALYSIS

Julius Stegmüller[1], Stefan Hayböck[1], Patrick Hartl[1] & Christian Breitsamter[1]

[1]Chair of Aerodynamics and Fluid Mechanics, Technical University of Munich, Boltzmannstraße 15, 85748 Garching,
Germany, julius.stegmueller@tum.de, Tel.: +49 89 289 16723

Abstract

Modern high-agility aircraft are often affected by the consequences of buffeting phenomena. At higher angles of attack, vortex bursting results in a strongly unsteady flow field downstream of the breakdown region. High turbulence intensities and their distinct burst frequency content lead to structural dynamic excitation of the wing and downstream located elements such as tail planes. Subsequently, heavy structural damage and degraded handling qualities may occur. Buffeting is an important numerical and experimental research field because of its complexity and criticality in future aircraft designs. A wind tunnel model has recently been developed at the Chair of Aerodynamics and Fluid Mechanics of the Technical University of Munich (TUM) for the experimental analysis of buffeting effects. The full-span model was designed based on the experience obtained from previous investigations on an aeroelastic half-span model. To ensure structural elasticity, the wings, the horizontal tail planes (HTPs), and the vertical tail planes (fins) are 3D-printed from polylactide (PLA). As roughly rigid reference cases, aluminum wings, HTPs, and fins can be mounted on the modular model configuration. The HTP's deflection angle can be adjusted by means of the HTP being rotatably mounted on the aluminum fuselage. In the context of this work, the aerodynamic characteristics as well as aeroelastic phenomena of the newly manufactured wind tunnel model are investigated experimentally. The focus lies on the analysis and comparison of the aerodynamic coefficients of the rigid and the flexible cases as well as on their sensitivities. Based on the experience gained from the force and moment measurements, signals of unsteady pressure transducers and accelerometers integrated into the lifting surfaces will be analyzed.

Keywords: Aeroelasticity, Flexible Wind Tunnel Model, Tail Buffeting

1. Introduction

Modern high-agility delta wing aircraft frequently experience buffeting at low to high subsonic Mach numbers and medium to high angles of attack. With increasing angle of attack, the vortex-dominated flow field shows increasingly unsteady features caused by sudden vortex bursting. The wake of bursting vortices contains high turbulence intensities with quasi-periodic pressure oscillations which interact with the aircraft structure. The coupling of aerodynamic excitation and structural response comprising the interaction of unsteady aerodynamic forces, inertia forces and elastic forces - with the unsteady aerodynamic forces related to local flow separation and lifting surface motion (vibrations) - is commonly referred to as buffeting. The structural response of the wing and tail planes affects the maneuverability of the aircraft, reduces the lifespan of structural components, and should therefore be avoided. The analysis and prediction of buffeting phenomena have been the subject of extensive research for a long time and are of great importance for the structural dynamic design of new aircraft in both the civil and military sectors. Numerical methods for predicting buffeting are continuously evolving due to increasing computing power, however they still need to be validated by wind tunnel tests. Therefore, wind tunnel models should have sufficient structural flexibility to make buffeting detectable, while being equipped with a reasonable number of sensors for data acquisition.

Davis Jr. and Huston formulated fundamental requirements and techniques for investigating buffeting on flexible wind tunnel models [1]. The authors compared damping characteristics, occurring vibrational modes, and reduced resonant frequencies of different wind tunnel models with those of a full-scale aircraft. They also suggested different methods of mounting models in the wind tunnel and how to avoid measurement errors. Rainey and Igoe indicated in their experimental studies on wing and tail buffeting that a quantitative transfer of buffeting loads from model to aircraft is only justified if structural dynamic scaling is applied [2]. The considered variables for scaling the model wing were dimensions, mass, moments of inertia, natural frequencies, and stiffness of the original wing. Therefore, the development of precise dynamically scaled models is complex and expensive. In the past, simple aeroelastic wind tunnel models often consisted of metal plates or spars covered with balsa wood [3, 4, 5]. More complex models were manufactured from carbon composites in an elaborate hand lay-up process [6, 7]. However, the honeycomb and foam cores of modern composite designs, which are difficult to model numerically, have a detrimental effect on the practicability.

Prior to the model discussed in this paper, the Chair of Aerodynamics and Fluid Mechanics of the Technical University of Munich developed an aeroelastic wind tunnel model (AWTM) of a half-span configuration [8]. A NACA 64A-005 airfoil was chosen for all lifting surfaces. To the authors' best knowledge, for the first time, a rapid prototyping process in combination with PLA filament was used to manufacture dynamically scaled lifting surfaces of the AWTM. A wing and HTP made of aluminum served as a more or less rigid reference case. The three main objectives of the AWTM are (i) the validation of the rapid prototyping manufacturing of flexible model parts, (ii) obtaining extensive experimental data from various configurations of both flexible and rigid wings and HTPs, and (iii) improving numerical buffeting prediction methods by validating numerical results on the basis of experimental data. The advantages of rapid prototyping are fast and cost-effective production as well as homogeneous material properties, which facilitate the structural modeling for numerical research. The aerodynamic and structural design of the AWTM was thoroughly tested in numerical studies [9, 10]. A ground vibration test (GVT) was performed on the wind tunnel model, which showed good agreement with predictions of an optimized FE model. Initial wind tunnel measurements of the pressure fluctuations on the wing and HTP confirmed the expected buffeting characteristics [8].
The $76°/40°$ double-delta wing planform has been extensively investigated in the scientific community. Verhaagen et al. studied the vortex flow over a rigid, sharp-edged $76°/40°$ double-delta wing model made of stainless steel [11]. The authors analyzed the vortex flow structure and its bursting behavior using smoke/laser-sheet flow visualization, surface oil-flow visualization, and static pressure measurements in combination with pressure-sensitive paint (PSP). The same $76°/40°$ double-delta wing planform was investigated by Cunningham Jr. et al. in a low-speed wind tunnel test campaign [12]. While the strake featured a sharp leading edge, a NACA 64A-005 airfoil was chosen on the outboard wing section. The wing model was instrumented with a six-component balance, accelerometers, and miniature pressure transducers to obtain forces and moments together with insights into the physics of vortex flow. Gonzalez et al. conducted wind tunnel tests on a sharp-edged $76°/40°$ double-delta wing planform with exchangeable fillets at the strake and wing juncture [13]. The authors performed measurements of forces and moments, surface static pressure measurements derived from taps and PSP, and smoke/laser-sheet visualization. A similar experimental setup was used by Woodiga et al who conducted detailed surface flow visualizations and force measurements on a $76°/40°$ double-delta wing with different junction fillets [14].

The newly developed aeroelastic full-span wind tunnel model (AWTMF) presented in this paper largely builds on the existing half model of the Institute. The full-span model differs from its half-span predecessor also by having fins and by its mounting mechanism. While the half model is installed on the wind tunnel floor, the full-span model is sting-mounted. Also, the number of integrated pressure and acceleration sensors increased considerably. Additionally, the full-span configuration allows the detection of asymmetric vibrational modes and enables buffeting analysis at different angles of sideslip. The manufacturing of flexible components by in-house 3D printers ensures maximum flexibility in the design process and results in the application of rapid prototyping for aeroelastic wind tunnel models.

The present paper is structured as follows. Section 2 describes the design concept of the aeroelastic wind tunnel model with its geometry parameters and the sensor positions and also the characteristic flow field of the selected design concept. In section 3, the measurement setup and the measurement conditions are explained. In Section 4, lift polars of the rigid configuration are discussed in comparison with results from the literature and the aerodynamic coefficients of the rigid and the flexible configuration are analyzed and compared. Subsequently, the measurement results of the transient pressure transducers and the accelerometers integrated in the wings, HTPs and fins are analyzed and compared for the flexible and the quasi-rigid reference case. Section 5 summarizes the results and gives an outlook.

2. Design Concept

An aeroelastic full-span model was developed for experimental analysis of buffeting effects by building on the experience gained with a wind tunnel half model [8]. The design concept is based on the idea that, on the one hand, a detailed flow-physical analysis of the occurring vortex systems and thus of the aerodynamic excitation can be carried out on a quasi-rigid configuration. On the other hand, the aeroelastic structural response of the wind tunnel model can be investigated on a configuration with flexible lifting surfaces. Consequently, the modularity of the wind tunnel model design is of great importance.

2.1 Modular Concept and Geometry

The modular design of the wind tunnel model consists of quasi-rigid lifting surfaces of aluminum and flexible lifting surfaces of PLA which can be attached to the rigid aluminum fuselage. The flexible components are scaled with respect to a possible generic large-scale configuration considering structural elasticity, i.e. especially wing and HTP deformation, and structural dynamics regarding wing and HTP bending and torsion modes, cf. similarity rules [15, 16, 17]. Figure 1 illustrates the modularity of the wind tunnel model. On the left hand side, the rigid components are depicted, on the right hand side, the flexible components are marked in lighter gray. The HTPs are rotatably mounted to the fuselage to allow different deflection angles.

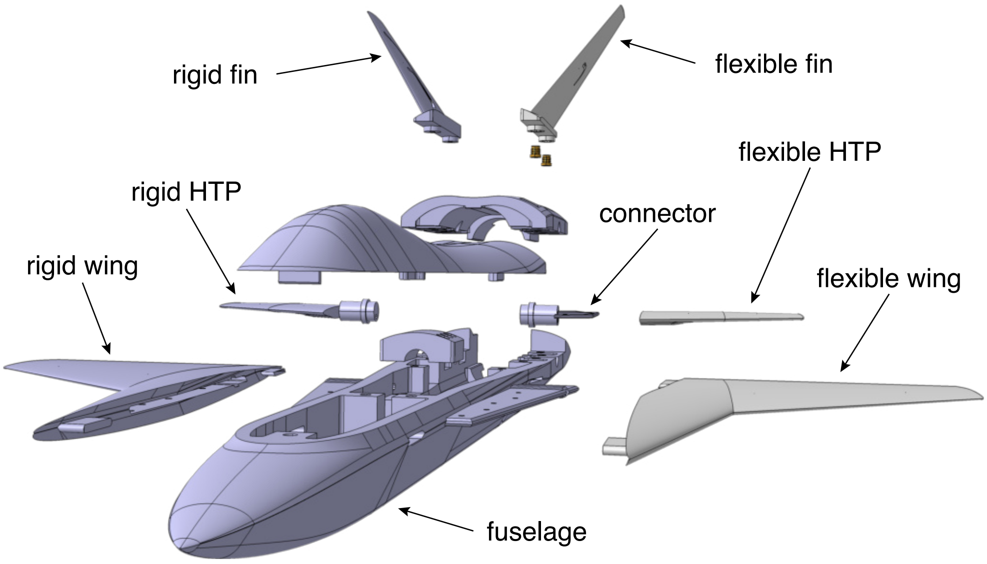

Figure 1 – Modular concept of the wind tunnel model

In contrast to the quasi-rigid HTP, which is manufactured in one piece, the flexible HTP is attached to an aluminum connector so that a strong clamping connection via the rear fuselage cover can also be provided for the flexible HTP. Table 1 shows the deflection δ_{HTP} associated with the respective angle of attack α used in the present investigation and reflecting possible trim conditions. The deflection angle δ_{HTP} is defined relative to the wing with positive values for nose-down deflection of the HTP.

Table 1 – Setting angle δ_{HTP} of the HTP with increasing angle of attack α

α	10°	15°	20°	22.5°	25°	27.5°	30°	35°	40°
δ_{HTP}	6°	10°	13°	14.5°	16°	17.5°	19°	22°	25°

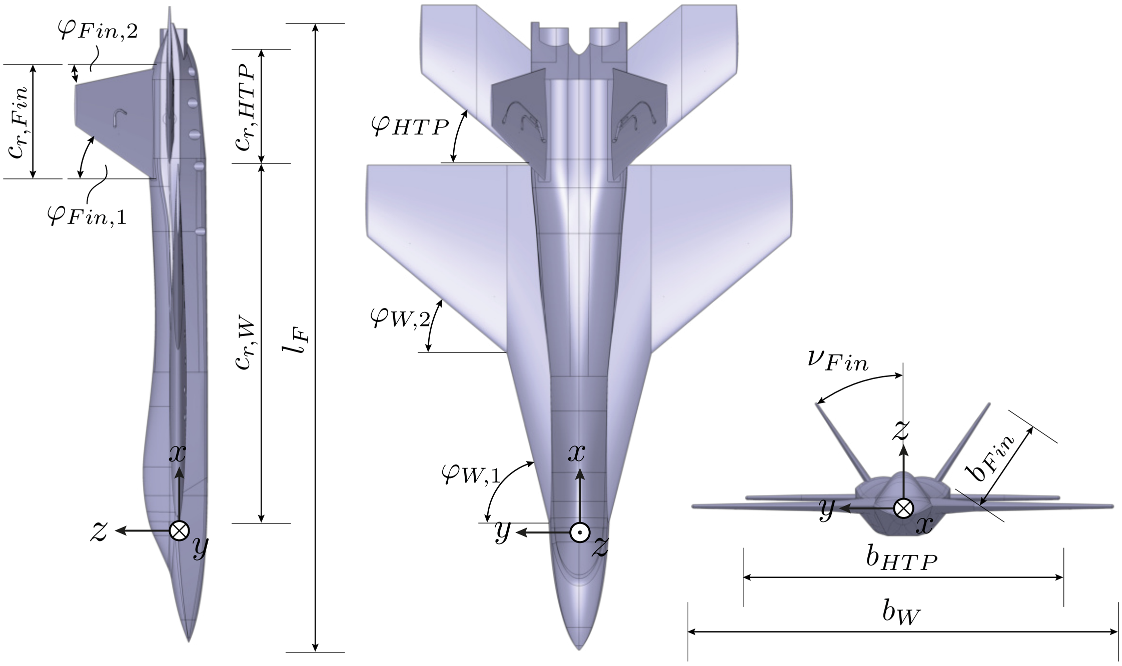

Figure 2 – Basic parameters of the wind tunnel model

Wing, HTP and vertical fin are all based on a NACA 64A-005 airfoil type. Figure 2 provides an overview of the model from different perspectives and also provides the basic model parameters. The dimensions and characteristic planform parameters of the wind tunnel model are given in Tab. 2. Identical to the half model developed by Katzenmeier et al. [8], the full-span model is characterized by a double delta wing with a sweep of $\varphi_{W,1} = 76^\circ$ at the strake and $\varphi_{W,2} = 40^\circ$ at the outboard wing section. The sweep angle of the leading and trailing edge of the HTP is $\varphi_{HTP} = 40^\circ$. The fins are deflected by $\nu_{Fin} = 34^\circ$ with respect to the x-z-plane. The leading edge of the fins features a sweep angle of $\varphi_{Fin,1} = 30^\circ$, whereas the trailing edge has a sweep angle of $\varphi_{Fin,2} = -10^\circ$.

Table 2 – Dimensions and characteristic planform parameters of the wind tunnel model

Wing/Fuselage		**HTP/Fin**	
l_F	$1.1\,m$	$c_{r,HTP} = c_{r,Fin}$	$0.2\,m$
l_μ	$0.427\,m$	$c_{r,HTP}/c_{r,W}$	0.3
$c_{r,W}$	$0.66\,m$	b_{HTP}	$0.55\,m$
b_W	$0.74\,m$	b_{Fin}	$0.17\,m$
$\varphi_{W,1}/\varphi_{W,2}$	$76^\circ/40^\circ$	$\varphi_{HTP}/\varphi_{Fin,1}/\varphi_{Fin,2}$	$40^\circ/30^\circ/-10^\circ$
S_{ref}	$0.25\,m^2$	ν_{Fin}	34°

Given a fuselage length of $l_F = 1.1\,m$, the model has a wing root length of $c_{r,W} = 0.66m$ and a wingspan of $b_W = 0.74m$. The mean aerodynamic chord is $l_\mu = 0.427\,m$ and the wing reference area measures $S_{ref} = 0.25\,m$. The root length of HTP and fin is identical with $c_{r,HTP} = c_{r,Fin} = 0.2m$. The HTP has a span of $b_{HTP} = 0.55\,m$. The span or rather the length of a fin is $b_{Fin} = 0.17\,m$, and it is measured as depicted in Fig. 2. In addition, the HTP's vertical position is offset by $0.015\,m$ in the positive z-direction relative to the wing plane, which provokes a higher vortex-induced turbulence intensity at the HTP.

2.2 Sensor System

To measure forces and moments as well as unsteady buffeting effects in the flow field, the wind tunnel model was instrumented with a six-component balance, transient pressure transducers (Kulites), and accelerometers (ACC). Figure 3 illustrates the positions of the sensors. Two Kulite pressure transducers (Kulite XCQ-093-5D) and an uniaxial accelerometer (PCB 352C22/NC) are installed on each wing, HTP, and fin. All sensors are located at the l/4-line of the respective lifting surfaces. The positions of the Kulites are marked with filled circles in Fig. 3, that of the ACC with a cross. Thus, in the case of the wing and the HTP, the pressure on the lifting upper surfaces can be measured at two positions. Kulite 1 refers to the inner position facing the fuselage, and Kulite 2 corresponds to the outer position on each side. Regarding the fin, the transient pressures are measured at an inward-facing position (Kulite 1) and at a location on the outer side (Kulite 2). The ACC are each located in the tip region of the wing, HTP, and fin, respectively. An additional ACC is placed in the symmetry plane of the fuselage in order to identify any dynamics transferred across the fuselage between individual lifting surfaces that do not result from the excitation of their specific eigenmodes.

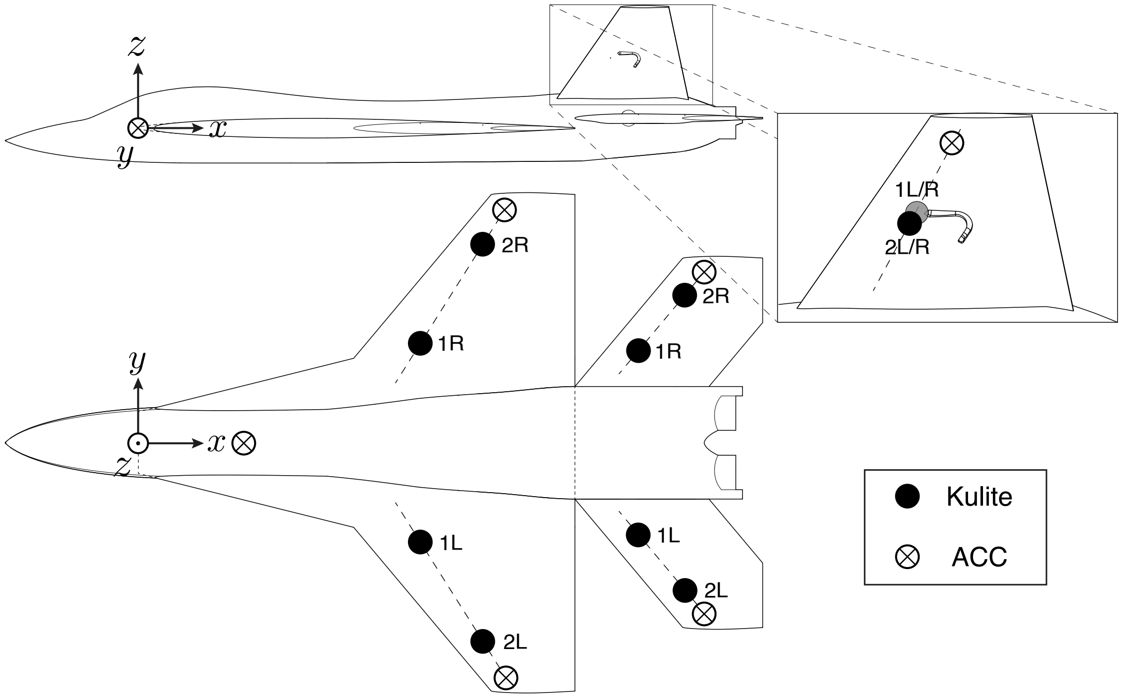

Figure 3 – Positioning of the pressure transducers (Kulite) and accelerometers (ACC) on the model

The exact positions of the sensors can be taken from Tab. 3. The origin of the body-fixed coordinate system concerning the x- and y- direction is located at the apex of the unblended wing planform at a distance of $190\,mm$ from the nose. In the z-direction, the origin is located in the wing plane. The x-positions are each referenced to the wing root length $c_{r,W}$. The y-positions at wing and HTP are related to their respective half span s_W and s_{HTP}. The spanwise positions of the sensors at the fin are referenced to the ratio of the value on the h-axis and the span b_{Fin}. The x-h-plane is rotated by $\nu_{Fin} = 34^\circ$ with respect to the x-z-plane. The ACC at the fuselage is located at $z_F = -34\,mm$ under the wing plane in the interior part of the fuselage.

Table 3 – Sensor positions

Sensor	$\frac{x_W}{c_{r,W}}\,[-]$	$\frac{\lvert y_W\rvert}{s_W}\,[-]$	$\frac{x_{HTP}}{c_{r,W}}\,[-]$	$\frac{\lvert y_{HTP}\rvert}{s_{HTP}}\,[-]$	$\frac{x_{Fin}}{c_{r,W}}\,[-]$	$\frac{h_{Fin}}{b_{Fin}}\,[-]$	$\frac{x_F}{c_{r,W}}\,[-]$	$z_F\,[mm]$
Kulite 1	0.651	0.400	1.144	0.500	1.081	0.475	-	-
Kulite 2	0.792	0.800	1.249	0.800	1.086	0.525	-	-
ACC	0.845	0.950	1.301	0.950	1.115	0.800	0.154	-34

2.3 Flow Field Classification

In the following, an overview of the basic flow physics of the delta wing design at low speeds will be given.

At the flow conditions of interest, two primary vortices are formed at the leading edge of each wing. Even at small angles of attack, the pressure-induced flow around the highly swept leading edge can no longer follow the wing contour and thus the boundary layers of the pressure and suction sides roll up with the entrained flow to form a large-scale leading-edge vortex. When fully developed, the inboard strake vortex extends up to the apex and rolls up along the leading edge of the strake. A second primary vortex (wing vortex) is formed at the kink of the leading edge. Its vortex axis is aligned to the lower sweep of the outer wing section. The vortex core is characterized by strongly increased axial velocities, low static pressure, and a high dissipation rate. Leading edge vortices also generate overspeeds at the wing surface, causing a higher suction peak, and thus, for delta wings, a non-linear increase in lift can be observed. Low static pressure in both vortex cores causes the strake vortex and the wing vortex to move towards each other and to start interacting. Figure 4 gives a simplified illustration of the vortex topology and vortex bursting points on a $76°/40°$ double-delta wing at $\alpha = 20°$ [11]. Vortex bursting is characterized by an abrupt divergence of vortex streamlines and a sudden increase in the vortex diameter. The flow field downstream of the bursting point is dominated by large-scale turbulent structures, which decay into smaller vortices and finally dissipate. With increasing angle of attack, the bursting locations move further upstream so that increasingly larger portions of the wings are affected by turbulence and produce less lift. On a $76°/40°$ double-delta wing, the wing-vortex is generally weaker and less stable than the strake-vortex due to the lower sweep of the outer wing section.

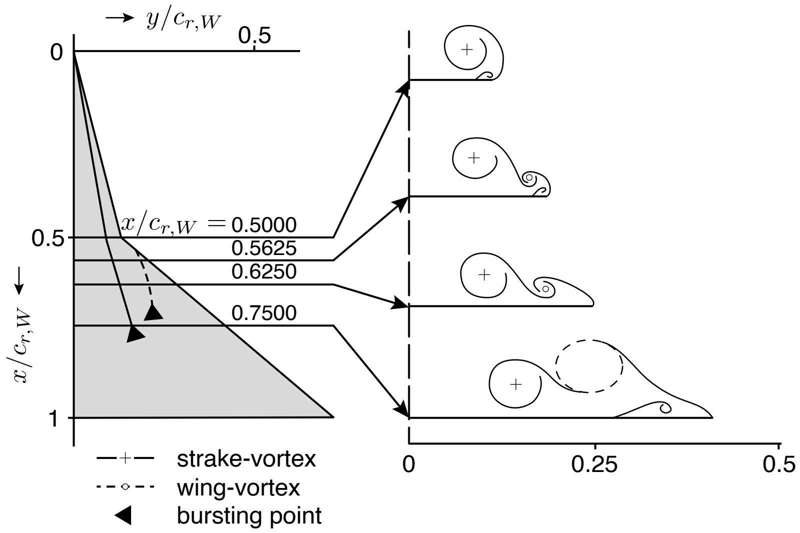

Figure 4 – Vortex topology on a $76°/40°$ double-delta wing at $\alpha = 20°$ adapted from Verhaagen et al. [11]

3. Experimental Setup

Wind tunnel measurements were performed with the quasi-rigid reference case (aluminum wings, aluminum HTPs and aluminum fins) and with the fully flexible version (PLA wings, PLA HTPs and PLA fins). The model is mounted on a two-axis support using a rear sting. This allows the adjustment of both the angle of attack and the yaw angle of the wind tunnel model. In order to introduce as little additional dynamic effects as possible into the system, the sting has no roll angle adjustment. Force and moment measurements with the internal six-component balance are performed separately from the measurements with Kulite and ACC. Instead of the balance a significantly stiffer dummy is used for the transient surface pressure and acceleration measurements. An inclinometer in the front area of the fuselage determines the absolute value of the angle of attack α. In the course of the present investigations, only the transient pressures and accelerations of the left hand side of the model are

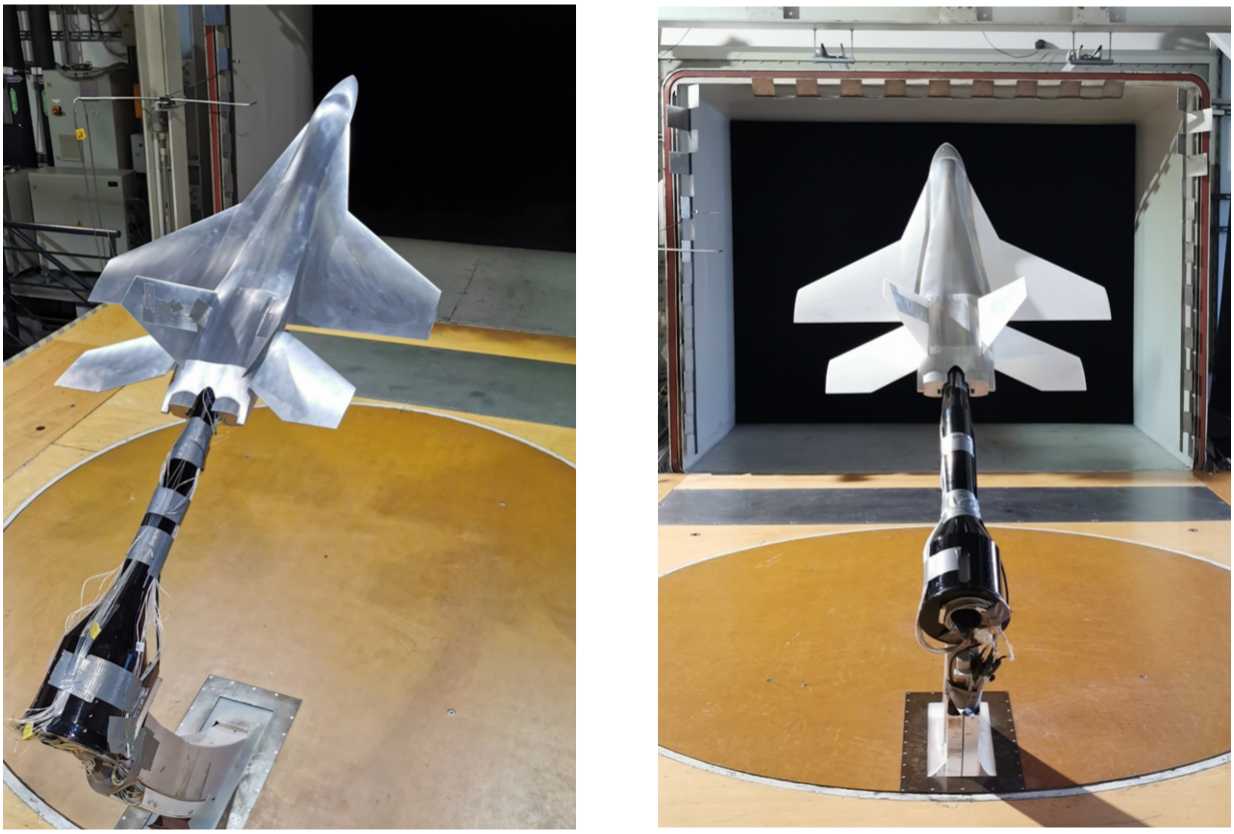

(a) Rigid configuration with integrated Kulites and ACCs

(b) Flexible configuration mounted on the internal six-component balance

Figure 5 – Wind tunnel model integrated in the test section

considered. Figure 5 shows both configurations integrated in the test section of the wind tunnel. The left hand side (Fig. 5a) shows the quasi-rigid configuration during the transient pressure and acceleration measurements. The right hand side (Fig. 5b) presents the flexible configuration during the force and moment measurements.

3.1 Measurement Setup

Self temperature compensation strain gauges are used as measuring elements in the internal six-component balance, which are connected in high spatial concentration to full bridges. The strain gauges are connected to a HBM MGCplus measuring amplifier system via HBM ML30B measurement cards. Figure 6 visualizes the measurement setup. The accelerometers are connected to a NI 9234 data acquisition card, the transient pressure transducers to NI 9237 data acquisition cards. The NI cDAQ-9185 chassis synchronizes the various measurements of all sensors and transfers the data to the LabView controlled computer. The wind speed is measured with a Prandtl probe in the freestream of the nozzle outlet. The measuring accuracy of the internal six-component balance relative to the total measuring range is 0.05% for the lift coefficient C_L, 0.1% for the drag coefficient C_D and 0.8% for the pitching moment coefficient C_{My}. For the transient pressure transducers, the combined measurement accuracy related to the non-linearity, hysteresis and repeatabilitly at maximum pressure is 0.5%. For the ACC, the measurement accuracy in terms of non-linearity is less than 1% and in terms of transverse sensitivity less than 5%.

3.2 Measurement Conditions

Both the force and moment measurements and the transient pressure and acceleration measurements were performed at the TUM-AER wind tunnel A, a Göttingen type wind tunnel. The cross section of the open test section of the wind tunnel has a dimension of $1.80m$ by $2.40m$ and the length of the test section is $4.80m$. With an open test section, the maximum speed is $65m/s$ with a turbu-

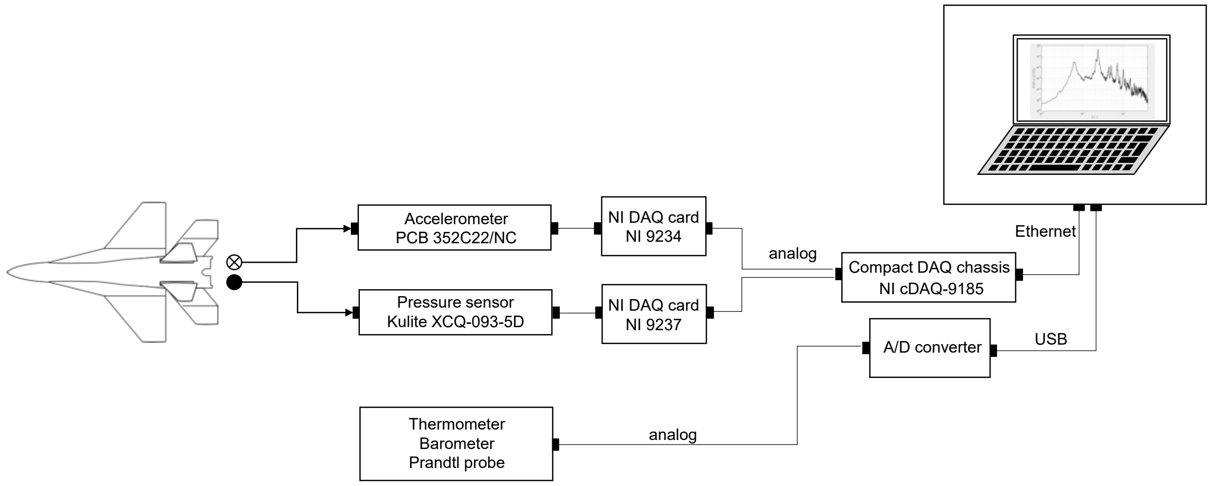

Figure 6 – Measurement setup

lence intensity in each coordinate direction of less than $0.4\,\%$. The measurement conditions can be found in Tab. 4. The Reynolds number related to the freestream velocity is set to $Re_{1/m} = 3.2 \cdot 10^6\,1/m$, which corresponds to a required freestream velocity of about $U_\infty = 51\,m/s$ and a Mach number of about $Ma_\infty = 0.15$. Thus, at all angles of attack fully turbulent boundary layers are present to form the large-scale leading-edge vortices. Measurements are performed in an angle of attack range between $\alpha = 10°$ and $\alpha = 40°$ with a measurement time of $10\,s$. The maximum model blockage at $\alpha = 40°$ is 5.6%. The sampling frequency of the force and moment measurements with the internal six-component balance was $f_s = 800\,Hz$. For the transient pressure and acceleration measurements, a sampling frequency of $f_s = 5120\,Hz$ was used. Thus, compared to the interesting range, where the first structural modes are up to approximately $f = 500\,Hz$, a 10 times higher sampling frequency was realized. A lowpass filter at half the sampling frequency $0.5 \cdot f_s$, which is automatically included in the data acquisition cards, avoids aliasing.

Table 4 – Wind tunnel measurement contitions

Parameter	**Value**
Mach number Ma_∞	$0.15\,[-]$
Reynolds number $Re_{1/m} = \frac{\rho_\infty U_\infty}{\mu}$	$3.2 \cdot 10^6\,1/m$
Freestream velocity U_∞	$51\,m/s$
Angle of attack α	$10° - 40°$

4. Results and discussion

In this section, first the results of the measurements with the internal six-component balance are presented and analyzed. Subsequently, the results of the Kulite and ACC measurements are discussed.

4.1 Forces and moments

The lift polar of modern high-agility aircraft configurations is characterized by an additional nonlinear lift component above a certain angle of attack and a higher maximum angle of attack. The fully developed leading edge vortices lead to an increase of the velocities on the wing upper surface and thus to a higher suction level. As the angle of attack increases, the vortex core structure changes and expands, which is known as vortex bursting. If the angle of attack is increased further, the bursting point moves further forward from the trailing edge and the affected area of the wing becomes larger. This leads to a reduction of the suction peak, and the lift decreases [18].

Figure 7a shows a comparison of the lift polars of four configurations of the rigid AWTMF wind tunnel model with the literature. The wind tunnel model equipped with (i) wing, HTP (deflection $\delta_{HTP} = 0°$) and fin, (ii) with wing and HTP ($\delta_{HTP} = 0°$) and (iii) with wing and fin is presented as well as (iv) the configuration with the wing only. The data taken from the literature for comparison are in each case flying-wing concepts without fuselage and a $76°/40°$ double-delta wing configuration. Cunningham Jr. et al. [12] used a symmetric double-delta wing with a diamond shape strake with a half top angle of $11.4°$ and a NACA 64A005 airfoil for the wing. Verhaagen et al. [19] and Gonzales et al. [13] conducted their measurements with a flat plate double delta wing with beveled sharp leading edges at the lower side, resulting in a slightly negative camber and a negative lift coefficient C_L for $\alpha = 0°$. Considering the different wing geometries and fuselage concepts, qualitatively the corresponding polar of the wing only configuration agrees well with the data from the literature. For all AWTMF configurations, vortex-induced nonlinear lift begins at about $\alpha = 8°$. The vortex breakdown over the wing leads to a sudden drop of the lift gradient at about $\alpha = 16°$. It is noticeable that the fin causes a significantly smaller increase in the lift coefficient from about $\alpha = 22°$ compared to the respective configuration with HTP or without HTP. The fins contribute to a negative lift increment from about $\alpha = 22°$, which results in a lower $C_{L,max}$.

In Fig. 7b the polars of the pitching moment coefficient of the four AWTMF configurations (wing/HTP/fin, wing/HTP, wing/fin and wing only) are shown. For the configurations with HTP, a steep increase in the pitching moment polar can be seen between $\alpha = 13°$ and $\alpha = 15°$. This occurs significantly earlier than the change in the lift polar from $\alpha = 16°$ onwards. The vortex breakdown has already reached the HTP at $\alpha = 13°$, which has a much stronger influence on the pitching moment coefficient than on the lift coefficient due to the larger lever arm. This is consistent with the fact that for the configurations without HTP, a stronger increase in the pitching moment coefficient is observed at a higher angle of attack of $\alpha = 15°$, which corresponds better to the breakdown of the lift increase at $\alpha = 16°$. Furthermore, it can be seen in Fig. 7b that for the two configurations with HTP, the presence of the fin in the angle of attack range between $\alpha = 20°$ and $\alpha = 33°$ generates an additional positive pitching moment compared to the configuration without the fin. This is consistent with the observation with the lift polars that the fin produces negative lift from about $\alpha = 22°$.

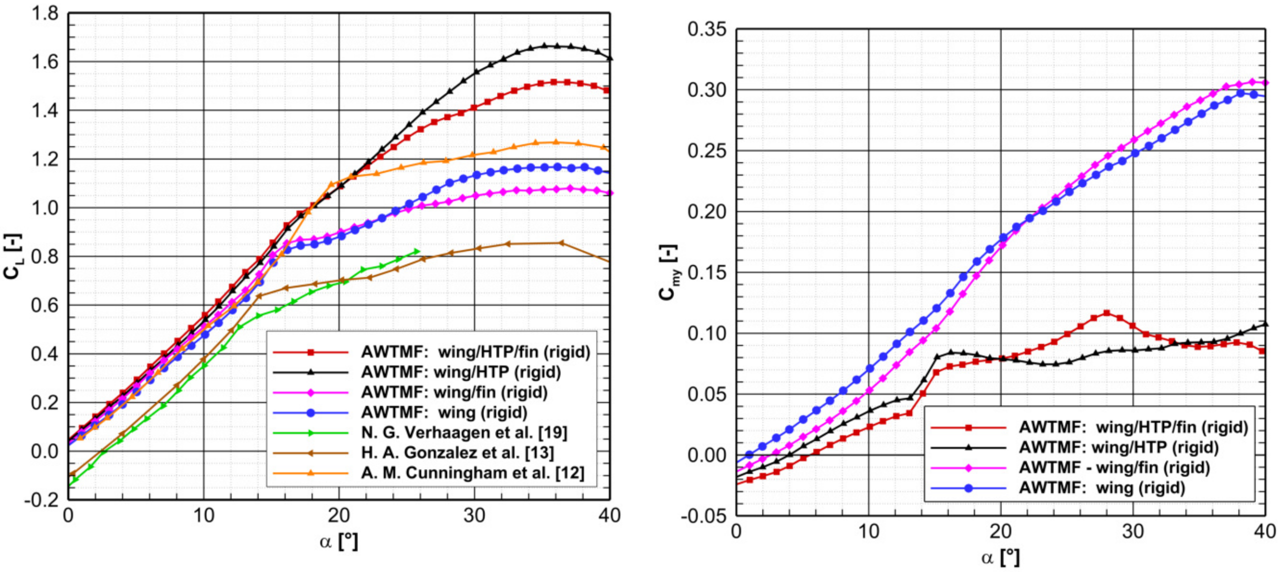

(a) Comparison of the lift coefficient of the AWTMF with the literature.

(b) Pitching moment coefficient of the AWTMF

Figure 7 – C_L and C_{My} of several $76°/40°$ double-delta wing configurations

Figure 8 shows a comparison of the lift coefficient C_L and pitching moment coefficient C_{My} of the flexible configuration (solid line) with the rigid reference case (dashed line) for different deflection angles of the HTP δ_{HTP}. In the following, always the full configurations with wing, HTP and fin are considered. Figure 8a demonstrates that as δ_{HTP} increases, the lift polars are shifted downward almost parallel to each other in most areas. The drop of the lift gradient resulting from the vortex breakdown can be identified at about $\alpha = 16°$ for deflection angles of the HTP between $\delta_{HTP} = 0°$ and $\delta_{HTP} = 16°$ and shifts to $\alpha = 15°$ for higher deflection angles. In this context, no significant deviations can be seen between the flexible and the rigid configurations for the lift polars.

In contrast, when comparing the pitching moment coefficients in Fig. 8b, significant differences between the flexible and the rigid reference configurations can be observed. Especially from an angle of attack of $\alpha = 20°$, the pitching moment coefficients of the flexible case are higher than those of the rigid reference case for comparable gradients C_{My_α}. From an angle of attack of $\alpha = 38°$ in the post stall region, the pitching moment coefficient gradients C_{My_α} also differ between the two configurations. In this case, the pitching moment coefficient C_{My} of the flexible case decreases significantly more than that of the rigid reference case. Overall, it can be seen that, unlike the lift polars, with increasing deflection angle δ_{HTP}, the pitching moment polars are shifted upward. Moreover, it is observed that in both cases the increasing pitching moment coefficient at $\alpha = 13°$ induced due to vortex bursting becomes larger with increasing deflection angle δ_{HTP} of the HTP. Thus, the pitching moment increase at $\delta_{HTP} = 0°$ is only about 64% of the increase at $\delta_{HTP} = 25°$. While the peak at $\alpha = 13°$ is more pronounced for higher deflection angles δ_{HTP}, the peak between $\alpha = 20°$ and $\alpha = 30°$ due to the additional negative lift of the fin is much more prominent for smaller deflection angles δ_{HTP}. Furthermore, this peak is shifted with increasing deflection angle δ_{HTP} to smaller angles of attack α.

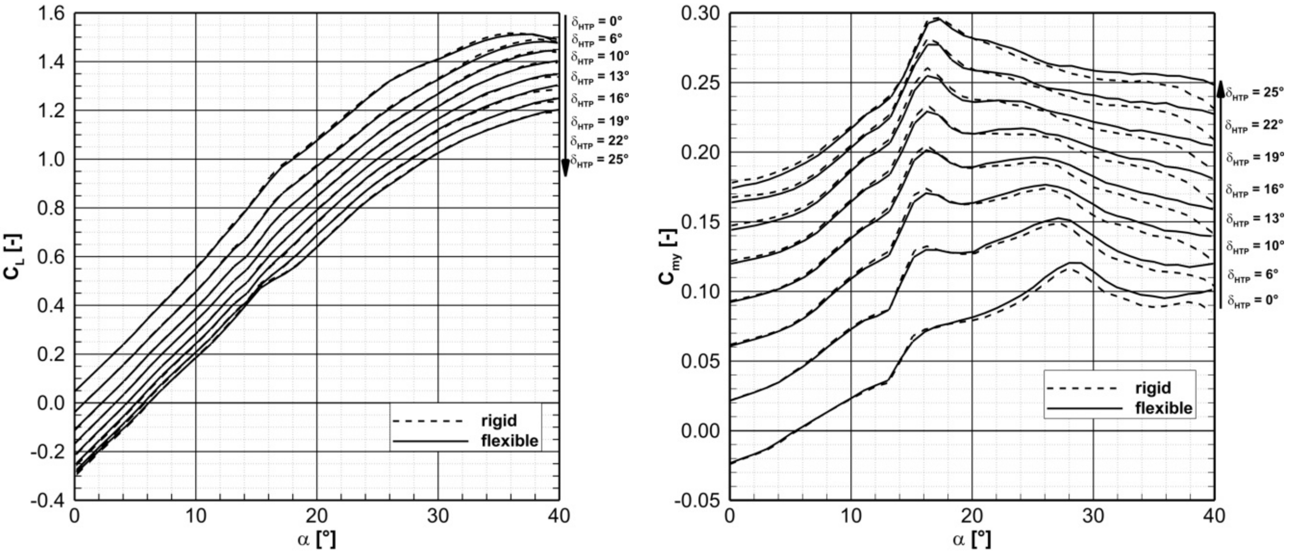

(a) Lift coefficient C_L

(b) Pitching moment coefficient C_{My}

Figure 8 – C_L and C_{My} of the rigid and the flexible configuration of the AWTMF for different deflection angles δ_{HTP} of the HTP

As with the lift polar, no significant differences are seen between the flexible and the rigid reference cases for the drag polar in 9a. While for $\alpha = 0°$ the drag raises with increasing deflection angle δ_{HTP}, it decreases for higher angles of attack since the deflection angle is defined relative to the wing and the HTP thus has a better alignment to the free flow referred to the drag. In addition, a drop in the gradient can be seen at about $\alpha = 16°$, which is more pronounced with higher deflection angles δ_{HTP} than with lower δ_{HTP} and recovers later at about $\alpha = 20°$. In the Lilienthal polar in Fig. 9b, this is reflected in a convex bulge starting at about $C_D = 0.2$. Again, no significant differences can be seen between the flexible and rigid configurations. As the deflection angle increases, the polar curve shifts to a lower C_L/C_D ratio.

In summary, it can be seen that there are no markable differences in the lift and drag polars between the flexible and the rigid reference configuration. However, for the more sensitive pitching moment polar it was found that the pitching moment coefficients in the flexible case, when vortex bursting has reached the trailing edge of the wing, are lower than in the rigid case and that in the post stall region even the gradients differ between the two configurations. In order to be able to precisely justify the observed and above described special characteristics in the curves of the individual polars and

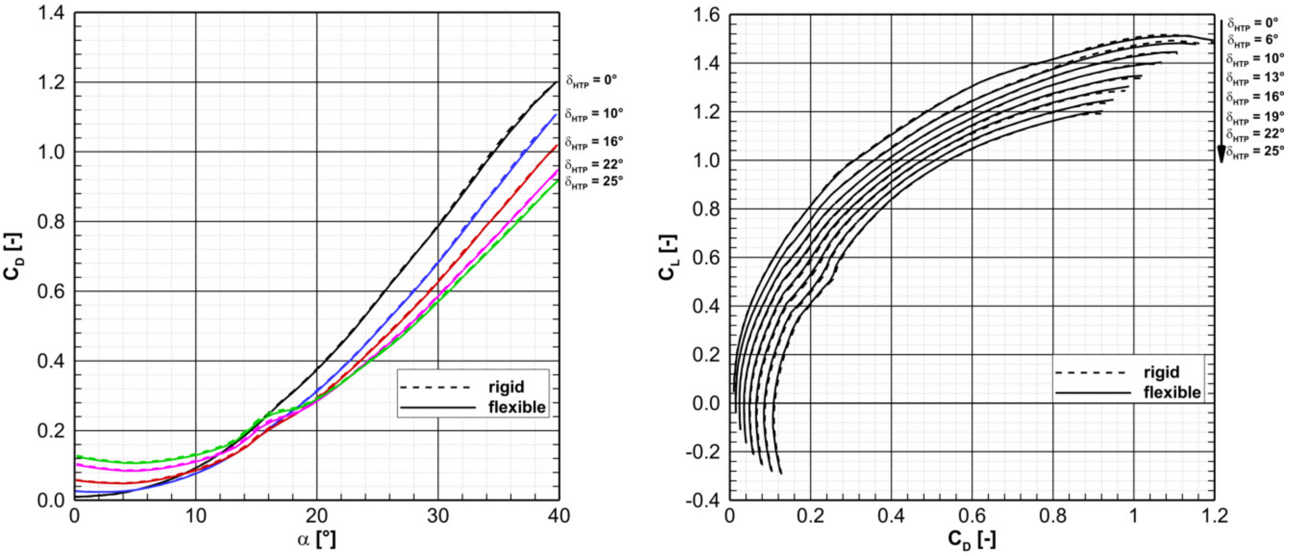

(a) drag coefficient C_D

(b) Lilienthal polar

Figure 9 – C_D and Lilienthal polar of the rigid and the flexible configuration of the AWTMF for different deflection angles δ_{HTP} of the HTP

to describe the flow field more accurately, simulations and PIV measurements will be performed in future investigations.

4.2 Surface pressures

For the measurements with the transient pressure transducers and accelerometers, the corresponding deflection angle of the HTP δ_{HTP} was set for each measured angle of attack α. The associated values can be found in Tab. 1. In the following, only the mean and rms values at the Kulite positions of the left wing, left HTP and left fin are considered. Figure 10 shows the curves of the mean pressure coefficients $\overline{c}_p$ at the Kulite positions for the flexible and the rigid configuration for an angle of attack range of $\alpha = 10°$ to $\alpha = 40°$. Figure 11 presents the rms values of the pressure coefficient $c_{p,rms}$ for the considered angles of attack. Considering the $\overline{c}_p$ values of the wing, in Fig. 10a it can be seen that at $\alpha = 10°$ they are lower at the outer Kulite position 2 than at the inner Kulite position 1. Due to the suction peak induced by the strake vortex, the tendency changes and $\overline{c}_p$ at Kulite position 1 located closer to the strake vortex decreases up to $\alpha = 22.5°$. If vortex bursting moves in front of the Kulite position, the mean value $\overline{c}_p$ and the rms value $c_{p,rms}$ increase. This agrees with the development of $c_{p,rms}$ in 11a, where there is a sudden increase of the rms value at position 1 starting at $\alpha = 22.5°$. Presumably due to the expected post stall region at $\alpha = 40°$, the pressure fluctuations in the form of $c_{p,rms}$ decrease. At Kulite position 2 the peak of the rms value is already reached at $\alpha = 27.5°$, but $c_{p,rms}$ rises already from $\alpha = 20°$ upwards and is at a higher level than at Kulite position 1. This indicates that the outer region of the wing is affected by vortex bursting earlier, but the inner region is subject to larger pressure fluctuations at higher angles of attack. The peak at Kulite position 2 for $\alpha = 15°$ is assumed to be caused by vortex bursting of the outer located wing vortex. Comparing the flexible and the rigid configuration, no significant differences can be seen in the mean values $\overline{c}_p$. However, there are clear differences in the rms values $c_{p,rms}$. Particularly for the inner position 1, the pressure fluctuations in form of $c_{p,rms}$ are larger for the rigid configuration than for the flexible one for most angles of attack. The largest differences are seen between $\alpha = 25°$ and $\alpha = 35°$, especially for $\alpha = 30°$. The pressure fluctuations at position 2 are very similar for the rigid case compared to the flexible case up to $\alpha = 22.5°$, then higher and lower from $\alpha = 30°$ upwards.

Also for the HTP, the $\overline{c}_p$ curves of the flexible case agree very well with the $\overline{c}_p$ curves of the rigid case. Even the curves at the two sensor positions differ only slightly in the range between $\alpha = 15°$ and $\alpha = 25°$ from each other, where slightly lower mean values can be seen at the inner position. For the remaining angles of attack the values of $\overline{c}_p$ are almost identical. While the mean pressure values rise into the positive range for $\alpha = 15°$, they then drop continuously to almost $\overline{c}_p = -0.7$ for

$\alpha = 40°$. The pressure fluctuations at the HTP in Fig. 11b are very similar for the flexible and the rigid case at both positions in the considered angle of attack range, with slightly lower $c_{p,rms}$ values from $\alpha = 27.5°$ upward for the rigid reference case. At the outer Kulite position, the $c_{p,rms}$ values are slightly higher for the rigid case for $\alpha = 22.5°$ and $\alpha = 25°$. Because the HTP is located downstream of the wing, it is affected by vortex bursting even at lower angles of attack. Thus, the pressure fluctuations in the form of the $c_{p,rms}$ values increase already for $\alpha = 15°$ upwards. While the $c_{p,rms}$ values at the inner position of the wing are only higher from $\alpha = 30°$ upwards compared to the outer position, this is already the case at $\alpha = 25°$ for the HTP. From $\alpha = 27.5°$ at the inner position and from $\alpha = 30°$ at the outer position, the pressure fluctuations decrease continuously again.

As for the wing and HTP, the mean pressure values $\overline{c}_p$ for the flexible and the rigid fin at both Kulite positions in Fig. 10c are almost the same. Compared to the force measurements, each angle of attack α was assigned to its own deflection angle of the HTP δ_{HTP} for the transient pressure measurements. Nevertheless, the curve of the mean pressure values $\overline{c}_p$ on the inside and outside of the fin at the specific Kulite positions supports the trend of the pitching moment polars in 7b that in the configuration with fin and HTP, the fin generates an additional downforce from $\alpha = 22°$ on. Regarding the mean pressure curves in Fig. 10c, it can be seen that, above $\alpha = 22.5°$, the $\overline{c}_p$ values at the outer Kulite position facing the HTP are lower than those at the inner position. Referring to these two Kulite positions this means a local downforce or negative lift. As with the HTP the pressure fluctuations in form of $c_{p,rms}$ for the fin in Fig. 11c increase already from $\alpha = 15°$ upwards. While the pressure fluctuations at the outer Kulite position 2 already decrease again beyond $\alpha = 27.5°$, the $c_{p,rms}$ value at the inner Kulite position 1 only decreases slightly above $\alpha = 30°$. Comparing the flexible and the rigid configuration, the higher pressure fluctuations at $\alpha = 27.5°$ at the outer Kulite position of the flexible fin are especially noticeable, while the values are almost identical for the inner position 1 and match those of the rigid case of the outer position 2. For the remaining angles of attack, the pressure fluctuations at both Kulite positions are very similar for the flexible and the rigid case, with slightly lower values for the flexible case for $\alpha = 22.5°$ and $\alpha = 25°$ and slightly higher values for $\alpha = 35°$ and $\alpha = 40°$.

In summary, the mean pressure values for wing, tail plane and fin surfaces considered show no significant differences between the flexible and the rigid configuration. Considering the aerodynamic excitation (buffet) related to the pressure fluctuations $c_{p,rms}$, slight differences can be observed between the flexible and the rigid configuration with very similar angle-of-attack dependencies. But the flexibility of the wing, of the HTP and of the fin seems to have an effect on the magnitude of the pressure fluctuations on the wing's, HTP's and fin's surfaces. In order to be able to analyze the differences and the specific characteristics of the curves in further detail, PIV measurements and numerical simulations will be performed in future studies to describe the flow field.

4.3 Vertical tip accelerations

In contrast to the aerodynamic excitation, significant differences between the flexible and rigid cases can be seen in the dynamic structural response. In Fig. 12, the dynamic structural response in terms of the vertical tip accelerations $a_{z,rms}$, normalized by the product of the inverse squared freestream velocity U_∞^2 and the root length $c_{r,W}$ is presented. The tip accelerations of wing, HTP and fin show a qualitatively similar curve for increasing angle of attack in the rigid case with quantitative differences mainly between $\alpha = 20°$ and $\alpha = 30°$. In this angle of attack range, the largest accelerations occur at the fin, the second largest at the HTP, and the smallest at the wing. Considering the flexible case, it can be seen that there are also qualitative differences between the individual components. Accordingly, as expected, the flexible components react significantly more sensitive to the aerodynamic excitation. For the flexible wing and flexible HTP, the tip accelerations for $\alpha = 15°$ are higher than for the rigid reference case, whereas for the fin, the accelerations in the flexible and rigid cases are more or less identical. Between $\alpha = 15°$ and $\alpha = 22.5°$ the tip acceleration increases very strongly with the flexible fin and decreases between $\alpha = 25°$ and $\alpha = 30°$ strongly and between $\alpha = 30°$ and $\alpha = 40°$ slightly. The accelerations of the wing and the HTP only increase more strongly at $\alpha = 20°$ but to a much lower level than those of the fin. While the accelerations of the wing decrease from $\alpha = 27.5°$, those of the HTP decrease slightly from $\alpha = 30°$ onwards. The sudden increase in tip accelerations at $\alpha = 20°$ in the case of the wing and the HTP, and at $\alpha = 15°$ in the case of the fin can be explained

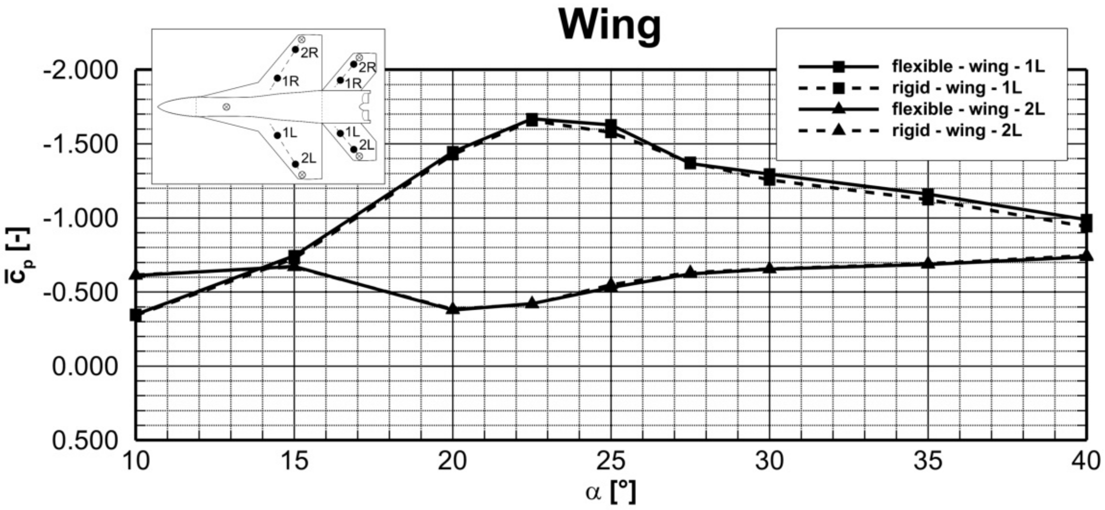

(a) $\overline{c}_p$ at the left wing

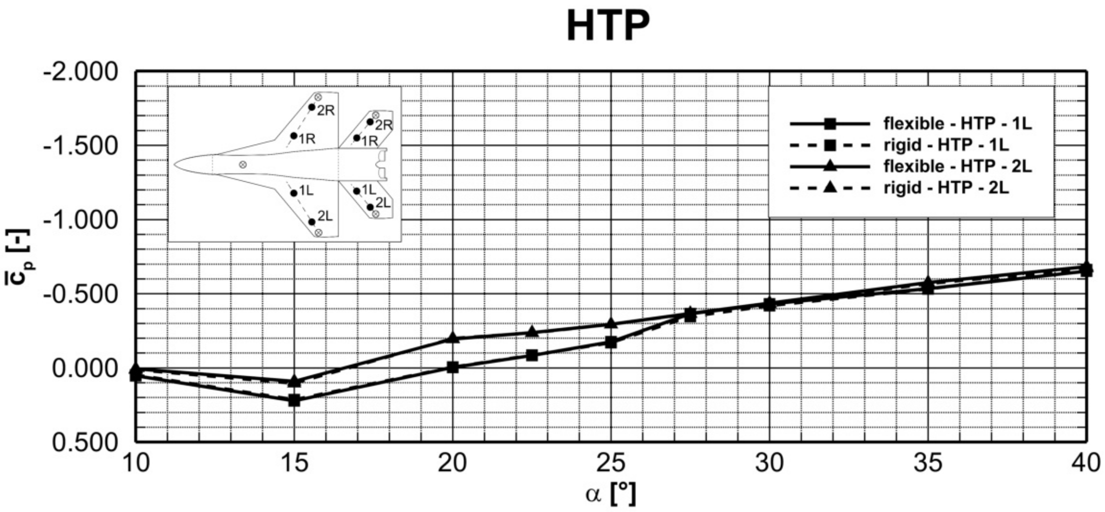

(b) $\overline{c}_p$ at the left HTP

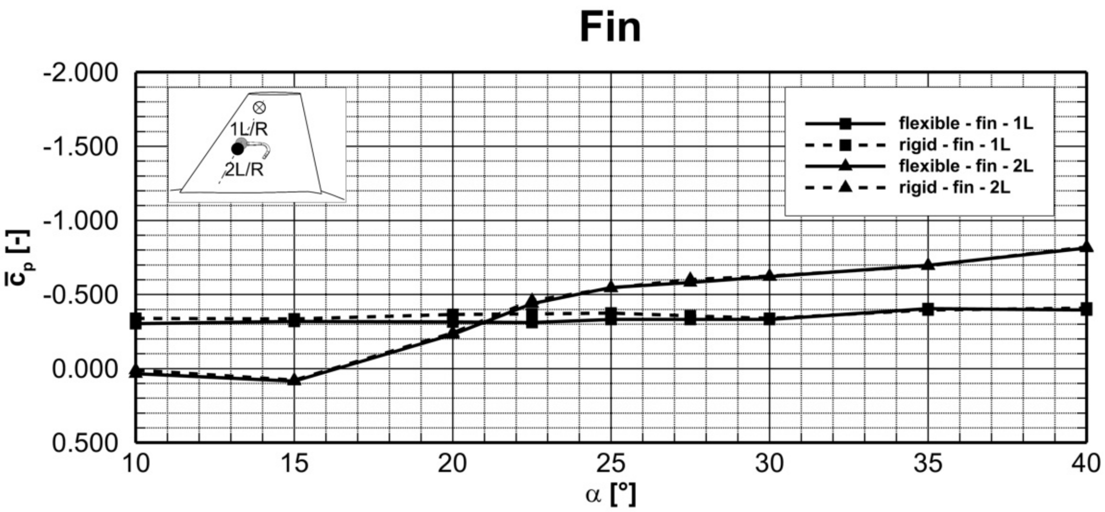

(c) $\overline{c}_p$ at the left fin

Figure 10 – Mean pressure coefficient $\overline{c}_p$ at the Kulite positions for the flexible and the rigid configuration

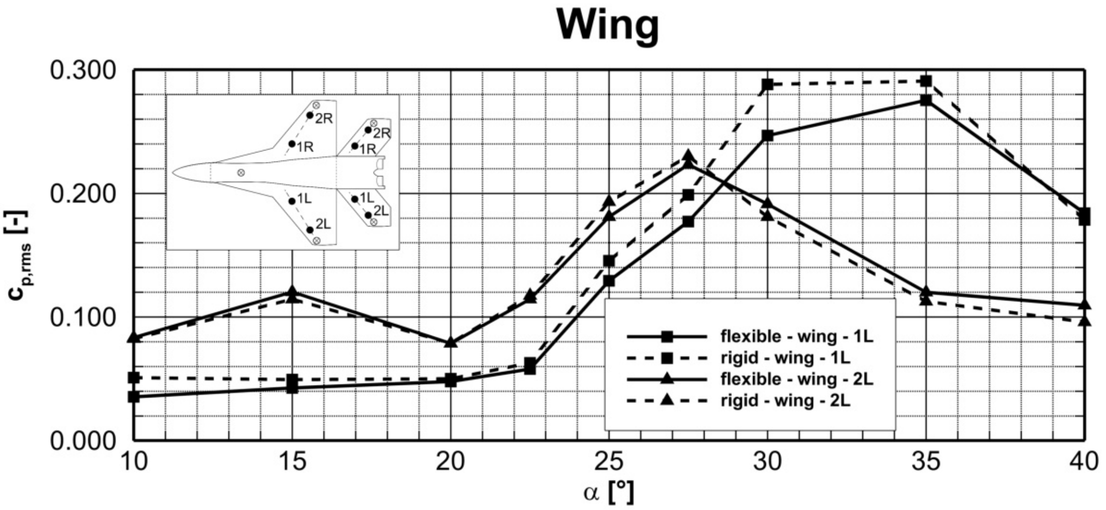

(a) $c_{p,rms}$ at the left wing

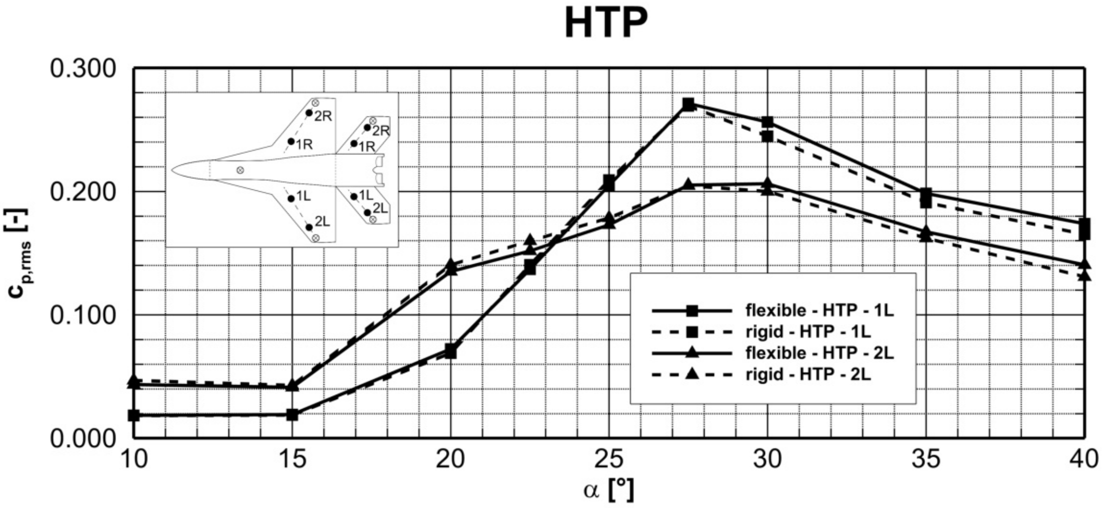

(b) $c_{p,rms}$ at the left HTP

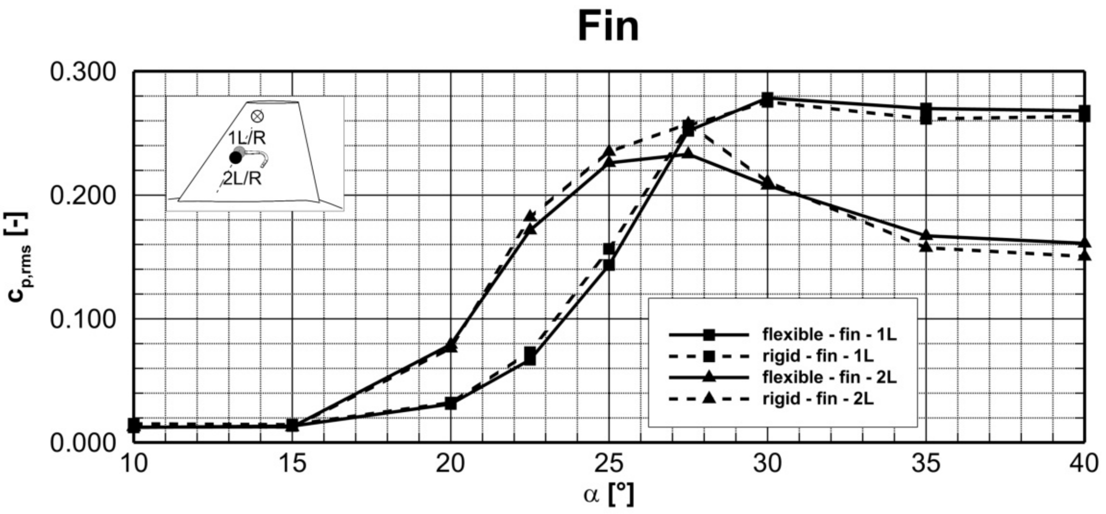

(c) $c_{p,rms}$ at the left fin

Figure 11 – Rms value of the pressure coefficient $c_{p,rms}$ at the Kulite positions for the flexible and the rigid configuration

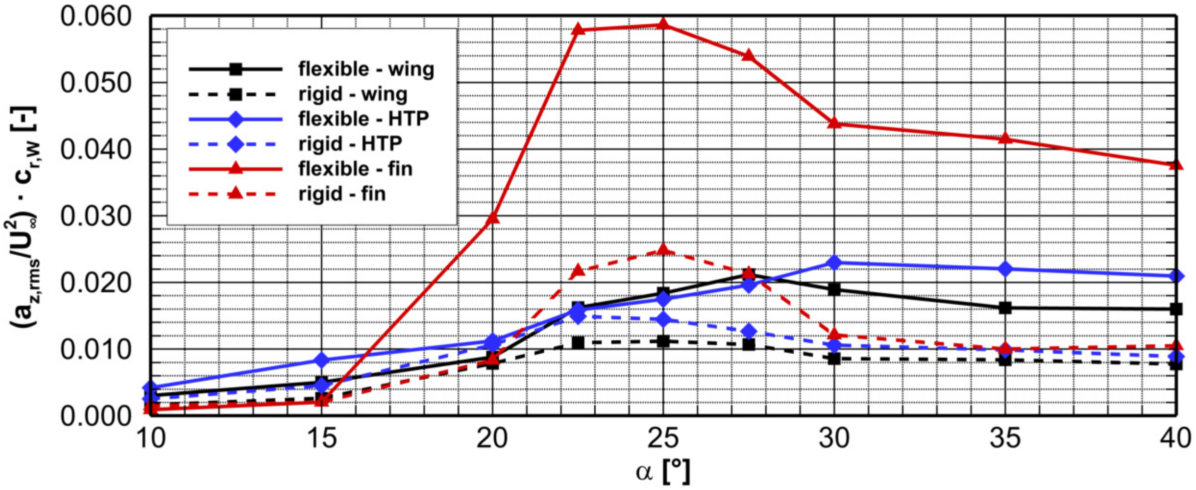

Figure 12 – RMS value of the vertical tip accelerations $a_{z,rms}$ of wing, HTP and fin for the flexible and the rigid configuration

by the vortex bursting. The burst vortical flowfield creates a strong impact on the fin(s) as the annular region of local turbulence maxima associated with the burst vortex system fully envelops the surfaces [18]. However, it can be observed that at a comparable aerodynamic excitation, significant differences in the dynamic structural response can be seen between the quasi-rigid and the flexible case. The flexible lifting surfaces are excited much more strongly and react more sensitive to occurring events in the aerodynamic excitation such as vortex bursting.

5. Conclusion

An aeroelastic full span wind tunnel model was developed for the experimental analysis of vortex induced buffeting effects. In the course of this study it was shown that the flexible model with its 3D-printed wings, horizontal tail planes and fins, together with the rigid aluminum reference model, is suitable for experimental investigations of buffeting. For this purpose, force and moment measurements were performed with an internal six-component balance. In addition, the model was equipped with unsteady pressure transducers to analyze the aerodynamic excitation (buffet) and with accelerometers to analyze the dynamic structural response (buffeting). It was observed that the lift polars agree well with the results from the literature and thus the model has typical characteristics of double delta wings with a sweep of $\varphi_{W,1} = 76^\circ$ at the strake and $\varphi_{W,1} = 40^\circ$ at the outboard wing section. It is shown that there are no significant differences in the lift and drag polars between the flexible and the rigid reference configuration for the different tail plane deflection angles. However, the more sensitive pitching moment coefficients are lower in the flexible case than in the rigid case after vortex bursting has reached the trailing edge of the wing and the gradients with respect to the angle of attack differ between the two configurations in the post stall region. The mean values of the pressures at the sensor positions at wing, HTP and fin are almost identical for the flexible and the rigid case. Considering the aerodynamic excitation (buffet) in the form of the pressure fluctuations, some differences between the flexible and the rigid configuration can be observed. Compared to the differences in the structural response (buffeting) measured with the accelerometers, the trends are nevertheless very similar. Thus, as it is generally expected, the tip accelerations and hence the structural response of the wing, the HTP, and the fin are significantly higher in the flexible case than in the rigid reference case over a wide range of angles of attack. Furthermore the flexible lifting surfaces react much more sensitive to occurring events in the aerodynamic excitation such as vortex bursting.

For a more detailed analysis of the individual polars of the aerodynamic coefficients and the averaged pressure values, pressure fluctuations and tip accelerations, further investigations must be performed also with regard to the comparison of the flexible and the rigid configuration. Further, numerical simulations and PIV measurements will be used to analyze the flow field. A ground vibration test is performed to be able to interpret the acceleration spectra. By mixing flexible and rigid lifting surfaces, upstream and downstream effects of the flexible components can be studied.

6. Contact Author Email Address

julius.stegmueller@tum.de

7. Funding

The project is funded by the Deutsche Forschungsgemeinschaft (DFG, German Research Foundation) grant number BR 1511/15-1.

8. Copyright Statement

References

[1] Davis Jr., D.D., Huston, W.B. The use of wind tunnels to predict flight buffet loads. Technical Report RM L57D25, National Advisory Committee for Aeronautics (NACA), Hampton, Virigina (1957).

[2] Rainey, G.A., Igoe, W.B. Measurements of the buffeting loads on the wing and horizontal tail of a 1/4-scale model of the X-1E airplane. Technical Report RM L58F25, National Advisory Committee for Aeronautics (NACA), Hampton, Virigina (1958).

[3] Triplett, W.E. Pressure measurements on twin vertical tails in buffeting flow. *Journal of Aircraft* 20(11), 920–925 (1983).

[4] Cole, S.R., Moss, S.W., Doggett Jr., R.V. Some buffet response characteristics of a twin-vertical-tail configuration. Technical Report TM-102749, National Aeronautics and Space Administration (NASA), Hampton, Virigina (1990).

[5] Bean, D.E., Wood, N.J. Experimental investigation of twin-fin buffeting and suppression. *Journal of Aircraft* 33(4), 761–767 (1996).

[6] Moses, R., Huttsell, L. Fin buffeting features of an early F-22 model. In: *41st Structures, Structural Dynamics, and Materials Conference and Exhibit*. American Institute of Aeronautics and Astronautics, Reston, Virigina (2000).

[7] Ringertz, U. Wing design for wind tunnel flutter testing. In: *International Forum on Aeroelasticity and Structural Dynamics (IFASD) 2019*, Savannah, Georgia (2019).

[8] Katzenmeier, L., Vidy, C., Kolb, A., Breitsamter, C. Aeroelastic wind tunnel model for tail buffeting analysis using rapid prototyping technologies. *CEAS Aeronautical Journal* 12, 633–651 (2021).

[9] Katzenmeier, L., Vidy, C., Benassi, L., Breitsamter, C. Prediction of horizontal tail buffeting loads based on URANS and DES approaches. In: *International Forum on Aeroelasticity and Structural Dynamics (IFASD) 2019*, Savannah, Georgia (2019).

[10] Katzenmeier, L., Vidy, C., Breitsamter, C. Using a proper orthogonal decomposition representation of the aerodynamic forces for stochastic buffeting prediction. Journal of Fluids and Structures 99 (2020).

[11] Verhaagen, N.G., Jenkins, L.N., Kern, S.B., Washburn, A.E. A Study of the vortex flow over 76/40-deg double-delta wing. Technical report, NASA Langley Research Center, Hampton, Virginia (1995).

[12] Cunningham Jr., A.M., den Boer, R.G., Dogger, C.S., Geurts, E.G.M., Persoon, A.J., Retel, A.P., Zwaan, R.J. Unsteady low-speed windtunnel test of a straked delta wing, oscillating in pitch. Technical report, National Aerospace Laboratory (NLR), Amsterdam, Netherlands (1988).

[13] Gonzalez, H.A., Erickson, G.E., McLachlan, B.G., Bell, J.H. Effects of various fillet shapes on a 76/40 double delta wing from mach 0.18 to 0.7. In: *RTO Applied Vehicle Technology Panel (AVT Symposium)*, vol. MP-069(I). Loen, pp. 4801–4839 (2001).

[14] Woodiga, S.A., Liu, T. Skin friction fields on delta wings. *Experiments in Fluids* 47(6), 897–911 (2009).

[15] Helmut, J. Critical review of methods to predict the buffet capability of aircraft. Technical Report AGARD Report No. 623, Messerschmitt-Bölkow-Blohm GmbH, Munich, Germany (1974).

[16] Huang, X.Z. Wing and fin buffet on the standard dynamics model. Technical report, Field Technology Inc, Long Beach, CA (2000).

[17] Butoescu, V.A.J. Similitude criteria for aeroelastic models. *INCAS BULLETIN* 7(1), 37–50 (2015).

[18] Breitsamter, C. Unsteady flow phenomena associated with leading-edge vortices. *Progress in Aerospace Sciences* 44(1), 48–65 (2008).

[19] Verhaagen, N.G. An experimental investigation of the vortex flow over delta and double-delta wings at low speed. In: *Aerodynamics of Vortical Type Flows in Three Dimensions (AGARD Conference Proceedings)*, vol. CP-342. Neuilly-Sur-Seine, pp. 701–716 (1983).